GSA Data Repository 2018016

Shen et al., 2018, Seismic evidence for lithospheric foundering beneath the southern Transantarctic Mountains, Antarctica: Geology, https://doi.org/10.1130/G39555.1.

## Methods Summary

Over 15 years of continuous seismic data from 216 stations (including the temporary seismic arrays TAMSEIS, GAMSEIS/AGAP, TAMNNET, POLENET/ANET, RIS/DRIS, and other national seismic networks such as: AI (Argentinean Italian Network), AU (Australian Network), C (Chilean National Seismic Network), ER (Mt Erebus Volcano Observatory Network), G (GEOSCOPE Network), GT (Global Telemetered Network), IU (Global Seismic Network), MN (Italian, Terra Nova Bay, TNV), PS (SYO, Japanese Syowa Station), YI (Antarctic Network of Broadband Seismometers), YN (Seismic Experiment in Patagonia and Antarctica), AW (Germany Stations), NORSAR (Norwegian base Troll) were downloaded and processed. Following Bensen et al., (2007), cross-correlation was performed to the vertical seismic components to obtain Rayleigh waves at periods between 8 and 50s. A frequency-time analysis (FTAN) was performed to fobtain inter-station Rayleigh wave phase and group travel time measurements, and then a linearized, damped and smoothed straight ray tomographic inversion (Barmin et al., 2001) was performed on these measurements. A quantitative comparison was performed between the phase speed maps constructed by ambient noise data and the earlier published maps derived from teleseismic earthquakes with a two-plane wave tomography method (Heeszel et al., 2016, Supplementary Fig. DR2). Similarities between the two sets of maps confirm the robustness of both results, and the quantitative differences help estimate the errors in both maps. Both sets of maps are combined to construct local dispersion curves. At periods both maps are available (26-50 sec), they are combined through a weighted summation scheme: a linear weight function is designed so that at 26 sec the ANT data is weighted 1 and 2PWT is weighted 0; and at 50 sec ANT data is down weighted to 0 and the weight of 2PWT is 1. The same weight function also applied to the uncertainty estimates of the phase speed.

A Bayesian Monte Carlo sampling algorithm was applied to individual local dispersion curves, and joint inversion of surface wave dispersion and P receiver function waveforms was performed at each station. An example of joint inversion for the station BYRD is shown in supplementary Fig. DR3. The resulting models at station locations are incorporated into the results from an inversion using only the surface wave dispersion alone. Estimates of the uncertainties of the resulting model were obtained by analyzing the posterior distribution of the model ensembles resulting from Bayesian Monte Carlo sampling. Examples of posterior marginal distributions for some key parameters discussed in the paper are shown in supplementary Fig. DR5. Details of the Monte Carlo inversion algorithm can be found in Shen et al., 2013. Supplementary Fig. DR4 presents the map views of the 3-D model at depths discussed in the main text. Additionally, Supplementary Fig. DR5a summarizes the crustal thickness of the resulting 3D model. Compared with the earlier models (supplementary Fig. DR5bc) the map reveals more structural variations in the new 3D model.

## Individual 1D Models at Different Geological Regions

For much of the study area only surface wave dispersion is used to constrain the 3D model. Supplementary Fig. DR6 presents the surface wave inversion results for three example points near the southern Transantarctic Mountains, East Antarctica, and the Ross Embayment in the West Antarctic. Substantial variations in the mantle structure is presented in the resulting model profiles. Posterior distributions for three selective attributes ($V_S$ at uppermost mantle depths (70-100 km) and at deeper depth (180-220 km), and the difference between the two) show that our surface data is providing robust constraints to them.

**Inferring Temperature of the Southern TAM**

In this study we infer the temperature (T) elevation in the uppermost mantle beneath the southern TAM from its anomalously low $V_S$ values. At ~80 km depth, the $V_S$ in the East Antarctica is ~ 4.55-4.6 km/sec (supplementary Fig. DR4). Given the pressure and shear velocity, following the method of Goes et al (2000), the temperature of the cratonic lithosphere at this depth is estimated ~800-850 °C. This value is consistent with other cratons and platforms (Priestley and McKenzie, 2006). Beneath the southern TAM, the slowest $V_S$ of ~4.15-4.2 km/sec at ~80 km depth corresponds to an uppermost mantle temperature of ~1250-1300 °C, computed by following Goes et al. (2000), or ~1350 °C by following Priestley and McKenzie (2006), considering the non-linear $V_S$-T relationship due to the increase of attenuation. As a result, we determine that if the low seismic speed beneath the southern TAM is solely due to higher mantle temperature, it at least requires a ~400-450 °C increase compared with the eastern Antarctica craton.

**Robustness Tests against Different Starting Q and $V_S$ models**

During the shear velocity inversion, we used a *Q* model (quality factor that quantifies the attenuation) to perform the physical dispersion correction to obtain the final $V_S$ model at 1 s period, but a high resolution Q model for this region is not available. In this study we set the *Q* to be a constant value of 150 in the upper mantle. beneath the southern Transantarctic Mountains, the replacement of cold lithosphere with warmer asthenosphere may cause an increase of attenuation (decreased *Q*) at shallow depths in the mantle. We test the robustness of our results with different attenuation models. Our test shows that, by decreasing *Q* from 150 to 75 in the uppermost 130 km of the mantle, it will increase the uppermost mantle $V_S$ by up to ~1%, which is smaller than the standard deviation of the posterior distribution (1.5%) (supplementary Fig. DR7). Thus different assumptions of the attenuation model do not alter our resulting images.

Due to the existence of the thick ice, the direct P-S phase in P receiver function waveforms for most of the seismic stations are dominated by ice sheet body wave reverberations. As a result, the depths to the subsurface seismic discontinuities (e.g., the Moho) can not be well constrained without specialized processing (e.g., Chaput et al., 2014). To test the robustness of our results against the high uncertainties in Moho depth, we performed a series of tests with different model spaces. Supplementary Fig. DR8 presents the marginal posterior distributions for the the average $V_S$ of the uppermost 50 km mantle with different allowances of Moho depth. The test shows that although such attribute is slightly affected by the prior constraints imposed to the inversion, but the effect is not strong enough to change our conclusion that the uppermost mantle beneath the southern TAM is substantially slow.

## Time Scale of the Lithosphere Foundering

Here in this section we describe how the timing scale of the lithosphere foundering is obtained from a simple calculation. Following Lee (2013), the calculation here is "encapsulated at the most rudimentary level in order to develop intuition" (cf. Davies,1999). Both the theoretical and numerical studies show that lithosphere foundering due to Rayleigh-Taylor-type instability or stepwise lithosphere structure (e.g., Houseman and Molnar, 1997; Stern et al., 2013) would initiate and grow with the time scale in the order of:

$$t \sim \frac{\eta_X}{\Delta\rho_X H g} \quad [1]$$

where $\eta_X$ represents the lithosphere viscosity, $\Delta\rho_X$ represents the density contrast between the cold fertile lithosphere and asthenosphere, $H$ is the thickness of the foundering layer, and $g$ is the gravity. Given the values listed in the main text: $\eta_X \sim 10^{22}$ Pa; $\Delta\rho_X \sim 0.03 \mathrm{g/cm^3}$; $H \sim$150-250km, we obtain the time scale $t$ to be ~4-7 m.a.. Stern et al. (2013) indicated that it takes >15$t$ to allow the viscous foundering to complete. Thus the simple calculation reveals a time scale of 60-100 m.a. for the lithosphere to complete. However, as we lack complete information about the extent of the foundered lithosphere, the accurate timing of the onset of the lithosphere foundering has large uncertainties.

## Supplementary References:


1. An, M., D. A. Wiens, Y. Zhao, M. Feng, A. A. Nyblade, M. Kanao, Y. Li, A. Maggi, and J.-J. Lévêque, *S*-velocity model and inferred Moho topography beneath the Antarctic Plate from Rayleigh waves, J. Geophys. Res. Solid Earth, 120, 359–383, doi:10.1002/2014JB011332 (2015).

2. Barmin, M.P., M.H. Ritzwoller and A. Levshin. A fast and reliable method for surface wave tomography. In *Monitoring the Comprehensive Nuclear-Test-Ban Treaty: Surface Waves* (pp. 1351-1375). Birkhäuser Basel (2001).

3. Bensen, G.D., M.H. Ritzwoller, M.P. Barmin, A.L. Levshin, Lin, F., Moschetti, M.P., Shapiro, N.M. and Y. Yang. Processing seismic ambient noise data to obtain reliable broad-band surface wave dispersion measurements. *Geophysical Journal International*, *169*(3), pp.1239-1260 (2007).

4. Chaput, J., R. Aster, A. Huerta, X. Sun, A. Lloyd, D. Wiens, A. Nyblade, S. Anandakrishnan, J. Winberry, and T. Wilson The crustal thickness of West Antarctica. *Journal of Geophysical Research: Solid Earth*, *119*(1), pp.378-395 (2014).

5. Davies, G.F. Dynamic Earth: Plates, plumes and mantle convection (2001).

6. Goes, S., R. Govers and P. Vacher. Shallow mantle temperatures under Europe from P and S wave tomography. *Journal of Geophysical Research: Solid Earth*, *105*(B5), pp.11153-11169 (2000).

7. Heeszel, D.S., D. Wiens, S. Anandakrishnan, R. Aster, I. Dalziel, A. Huerta, A. Nyblade, T. Wilson and P. Winberry. Upper mantle structure of central and West Antarctica from array analysis of Rayleigh wave phase velocities. *Journal of Geophysical Research: Solid Earth* (2016).

8. Houseman, G.A. and Molnar, P., 1997. Gravitational (Rayleigh–Taylor) instability of a layer with non-linear viscosity and convective thinning of continental lithosphere. *Geophysical Journal International*, *128*(1), pp.125-150.

9. Lee, C.T. Compositional variation of density and seismic velocities in natural peridotites at STP conditions: Implications for seismic imaging of compositional heterogeneities in the upper mantle. *Journal of Geophysical Research: Solid Earth*, *108*(B9) (2003).

10. Priestley, K. and D. McKenzie. The thermal structure of the lithosphere from shear wave velocities. *Earth and Planetary Science Letters*, *244*(1), pp.285-301 (2006).

11. Shen, W., Ritzwoller, M.H. and Schulte-Pelkum, V., 2013. A 3-D model of the crust and uppermost mantle beneath the Central and Western US by joint inversion of receiver functions and surface wave dispersion. *Journal of Geophysical Research: Solid Earth*, *118*(1), pp.262-276.

12. Stern, T., G. Houseman, M. Salmon and L. Evans. Instability of a lithospheric step beneath western North Island, New Zealand. *Geology*, *41*(4), pp.423-426 (2013).

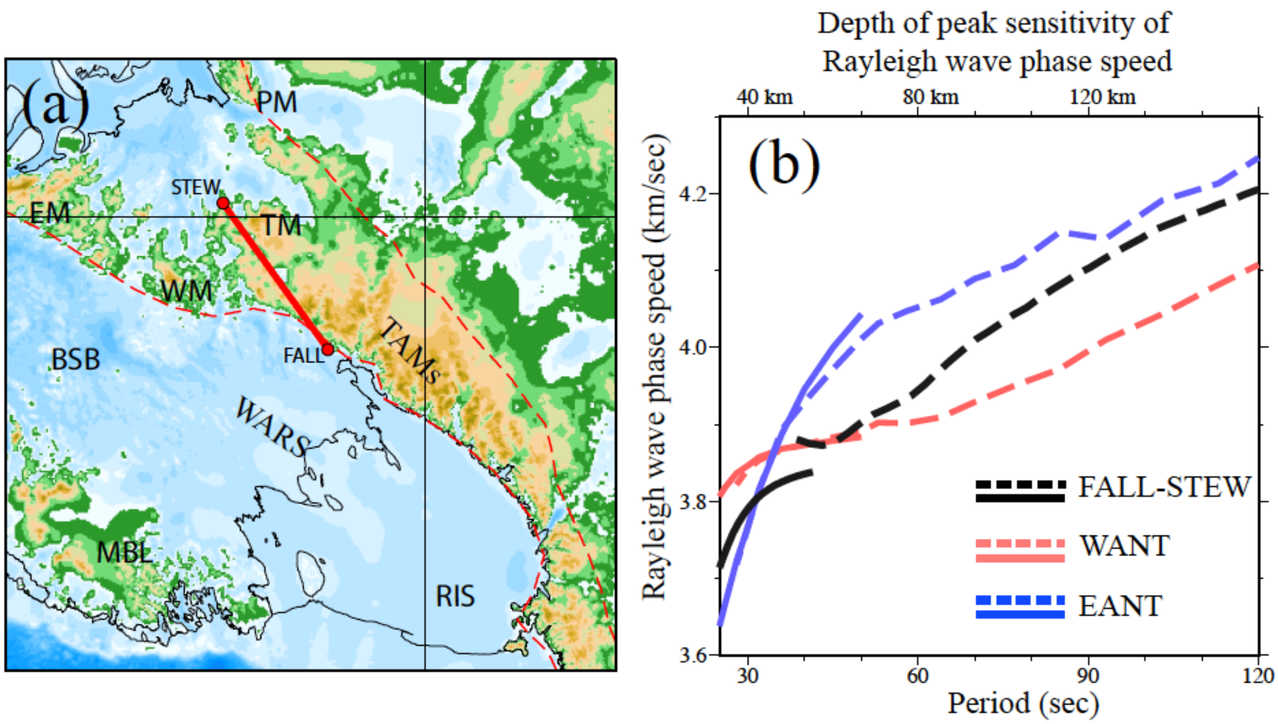


**Supplementary Figure DR1.** Direct evidence of a slow uppermost mantle beneath the southern TAM. (a) Locations of the POLENET/ANET stations STEW and FALL. (b) Phase speed dispersion curves at station pair FALL-STEW are shown as black solid lines (ambient noise measurements) and dashed line (teleseismic two-station measurements). For comparison, the average dispersion for the East Antarctica and West Antarctic are also shown. The approximate peak depth of the of the Rayleigh wave phase speed sensitivity for different periods are also marked in the plot.

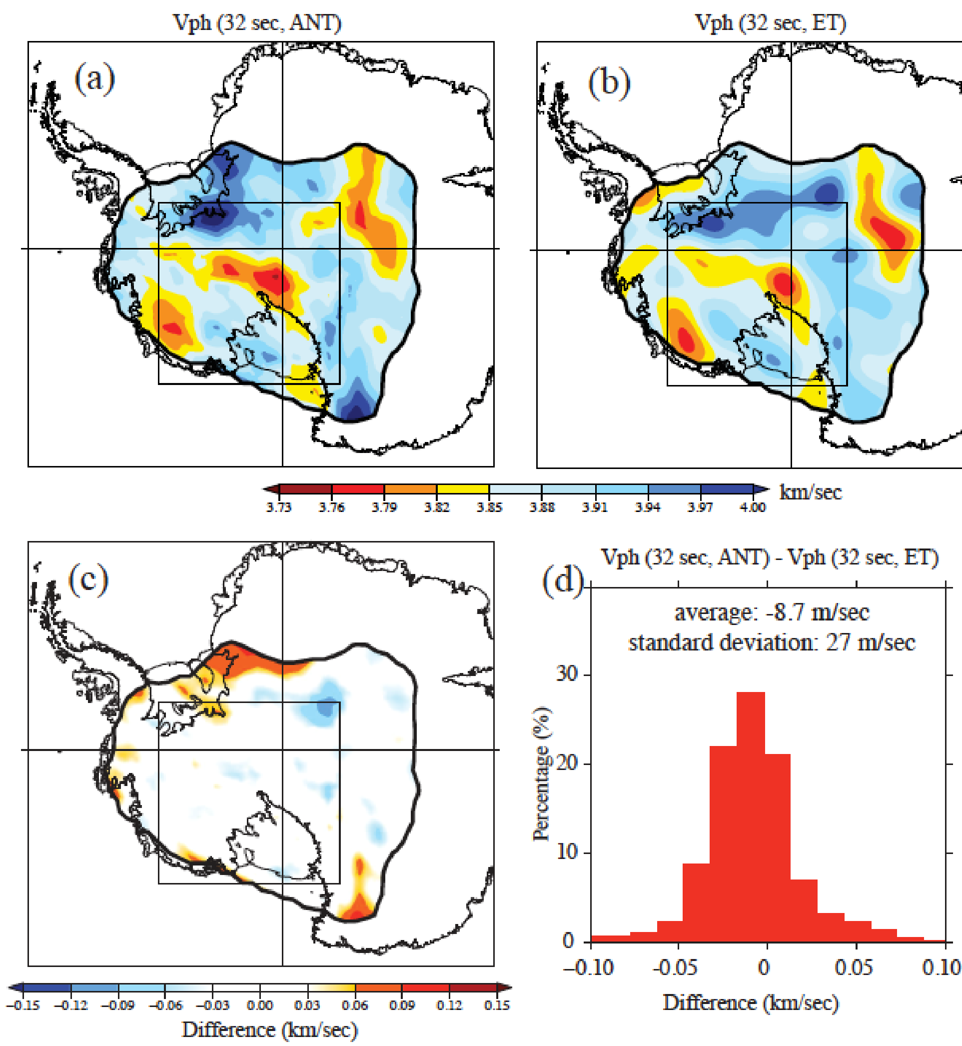


**Supplementary Figure DR2.** Comparison of ambient noise derived Rayleigh wave phase speed map and those produced from teleseismic earthquakes. (a-b) 32 sec Rayleigh wave phase speed map from ambient noise tomography (ANT) and earthquake tomography (ET), respectively. The black box shows our focus region of this paper. (c) Difference between (a) and (b). (d) Histogram of the difference between two maps in our focus region. The average difference is ~ 9 m/sec (~0.25%), and the standard deviation is ~27 m/sec (~0.7%). On average, maps derived from earthquakes are only slightly faster than those from ambient noise.

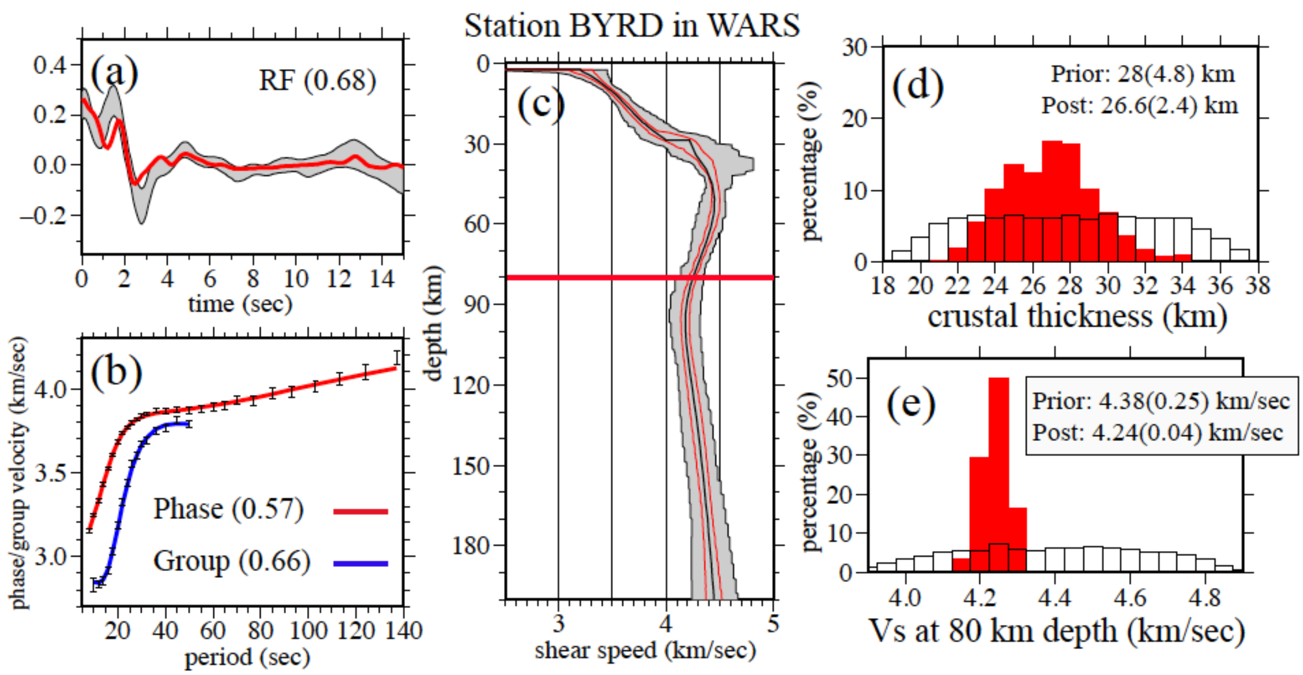


**Supplementary Figure DR3.** Example Monte Carlo joint inversion of surface wave dispersion and receiver functions for station BYRD. (a) Observed receiver function (RF) with uncertainties are shown with the grey corridor. The red curve represents the synthetic RF from the model shown as the black profile in (c). The square root of the reduced $\chi^2$ misfit to the observed RF is 0.68. (b) Observed phase and group speed dispersion curves for BYRD is shown as black error-bars. The fit from the average model to the observed data is shown as red and blue curves for phase and group speeds, respectively. (c) The resulting 1D shear speed ensemble. Black profile represents the average model, while the two red profiles represent the 1 standard deviation of the posterior distribution. The full model ensemble fills the grey corridor with black outlines. (d) Prior and posterior distributions for the crustal thickness are shown as red and blank distribution, respectively. Mean and standard deviation for these distributions are attached. (e) Same as (d), but represents the marginal distributions for the $V_S$ at 80 km depth (marked by the red line in (c)).

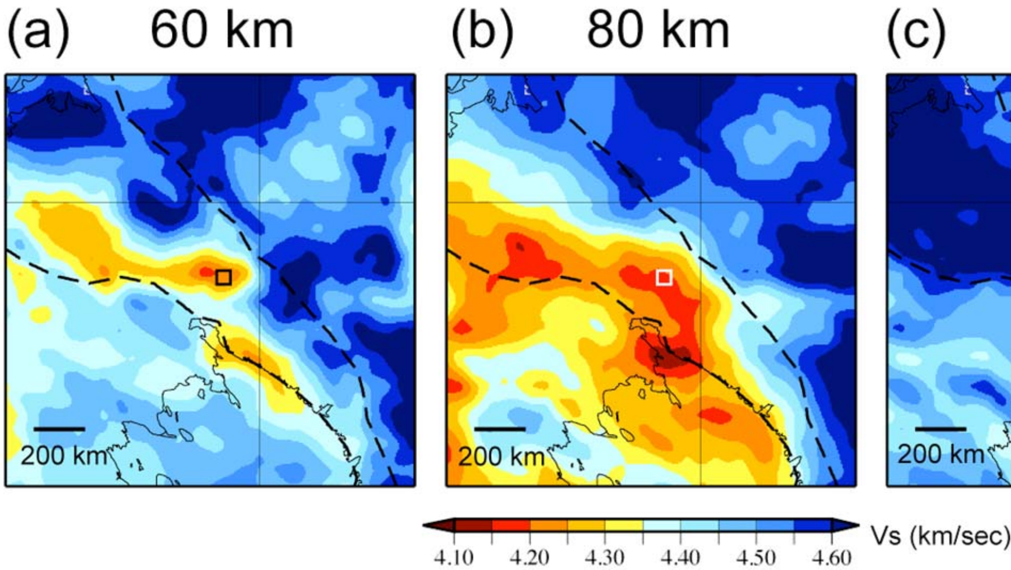


**Supplementary Figure DR4**. (a-c): Map views of absolute shear speed at depths of 60, 80, and 200 km, respectively. Small boxes indicate the location of the Mount Early/Sheridan Bluff.

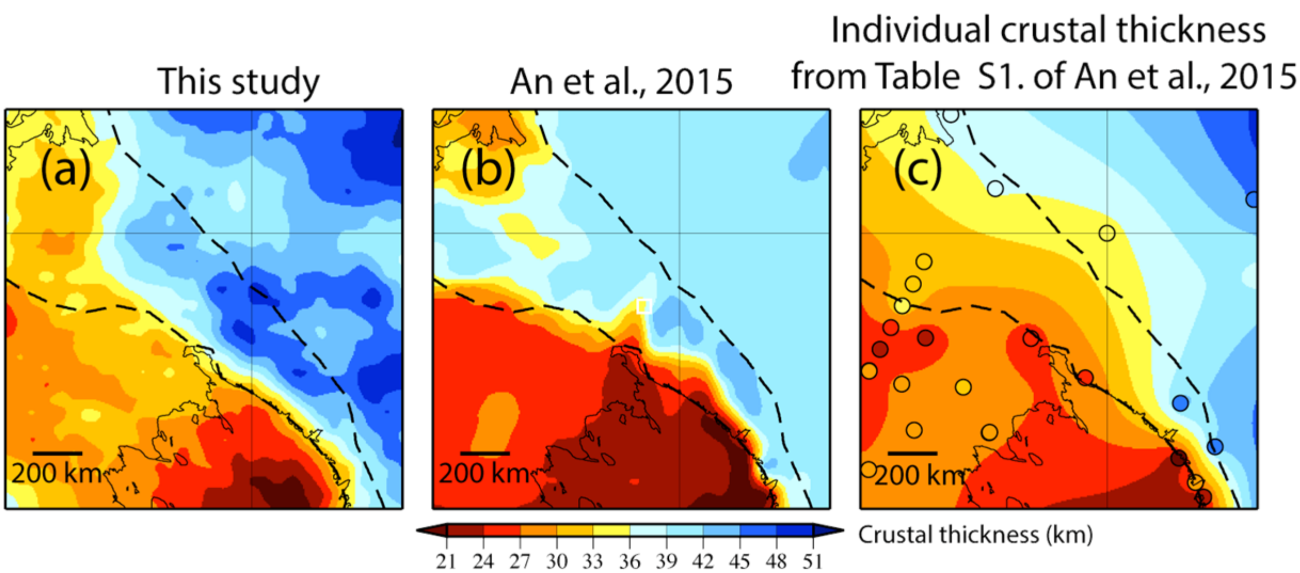


**Supplementary Figure DR5**. Crustal thickness of the study region**.** (a) Crustal thickness from this study. (b) Crustal thickness from the 3D model constructed by An et al., 2015; (c) Crustal thickness mapped by receiver function studies at individual stations from the Table S1 from An et al., (2015), collected from seismic studies such as Chaput et al., 2014.

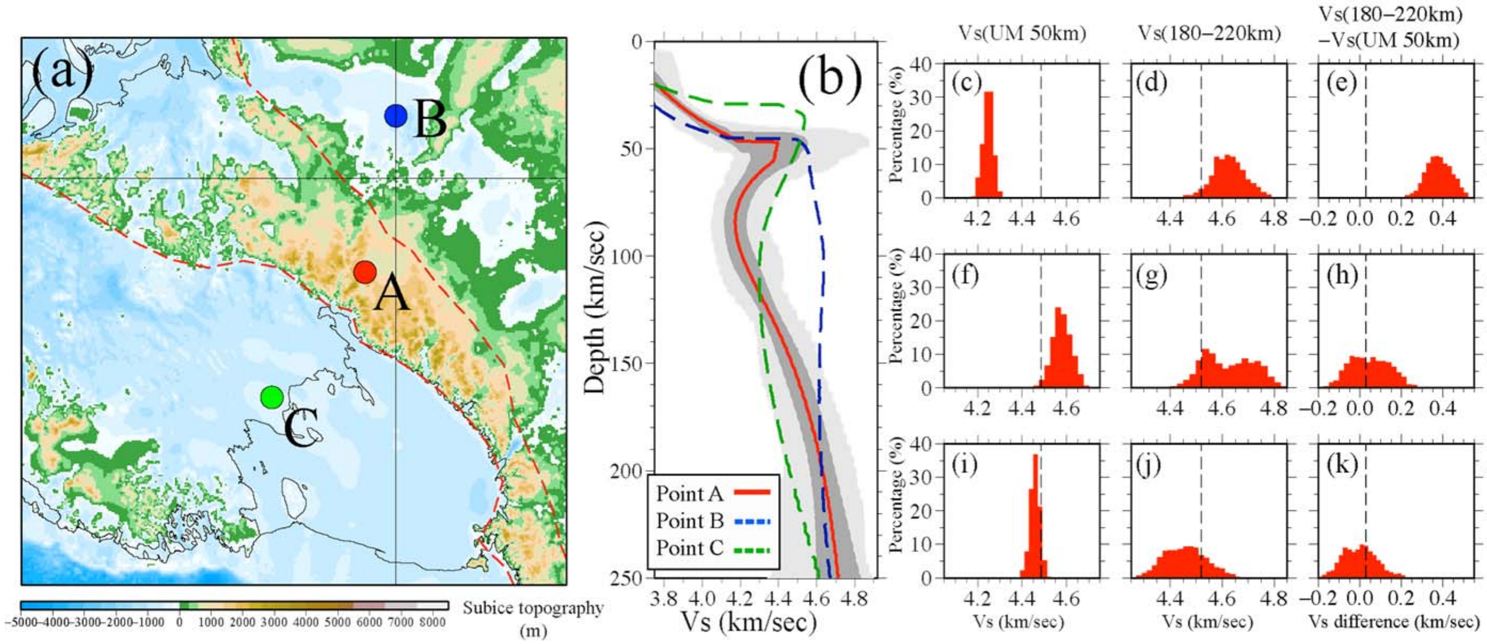


**Supplementary Figure DR6.** Example of posterior distribution for select attributes. (a) Locations of example points. Point A is located in the southern Transantarctic Mountains, while Points B and C are located in the East Antarctic and the Ross Embayment, respectively. (b) Resulting 1D models for the points A, B, C are shown as red, blue, and green lines, respectively, constrained by the surface wave dispersions. For Point A, the 1 standard deviation for the resulting model ensemble is shadowed by dark grey corridor, and the full expansion of the resulting model ensemble is shown as light grey corridor. (c-e) Marginal posterior distributions for attributes of average $V_S$ in the uppermost 50 km of mantle (UM 50 km), 180-200 km depth range, and difference of the two $V_S$, respectively, for Point A. (f-h) Similar to (c-e), but for Point B in the East Antarctic. (i-k) Similar to (c-e), but for Point C in the West Antarctic Rift System. The dashed lines in (c-k) represent the global average values for these attributes (taken from the AK135 reference model).

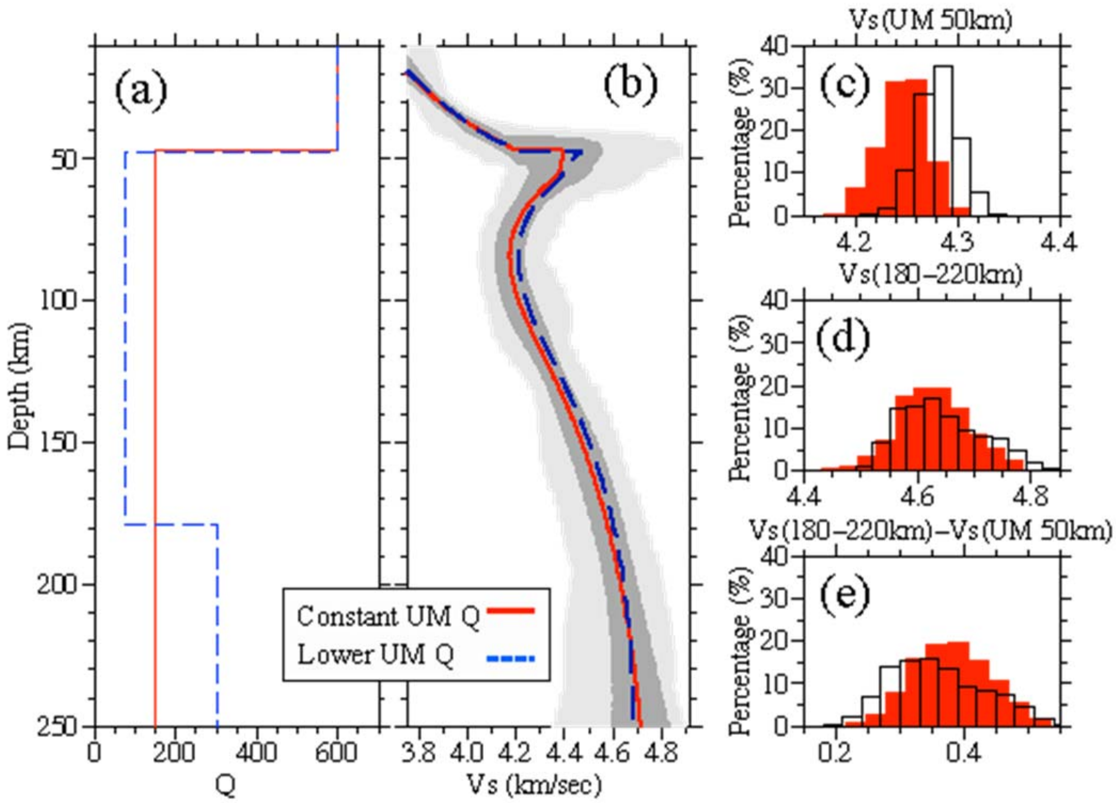


**Supplementary Figure DR7**. Robustness test against different attenuation (Q) models. (a) Two different Q models. The red solid Q model is used to construct the 3D model, which represents a constant Q (Q=150) in the uppermost mantle. Blue dashed profile is a depth-variant Q model in which Q at depths < 180 km is 75 and increases to 300 at greater depths. (b) Resulting average model (red line), 1 standard deviation (dark gray corridor), and full model ensemble (light gray corridor) from inversion with constant mantle Q model for point A whose location is shown in Sup. Fig. DR6a. The average model from inversion with depth variant Q model is shown as a blue dashed profile. (c-e) Marginal posterior distributions for three key attributes discussed in the paper from the constant mantle Q inversion are shown as red histograms. The posterior distributions for inversion with depth-variant Q model are shown as open histograms.

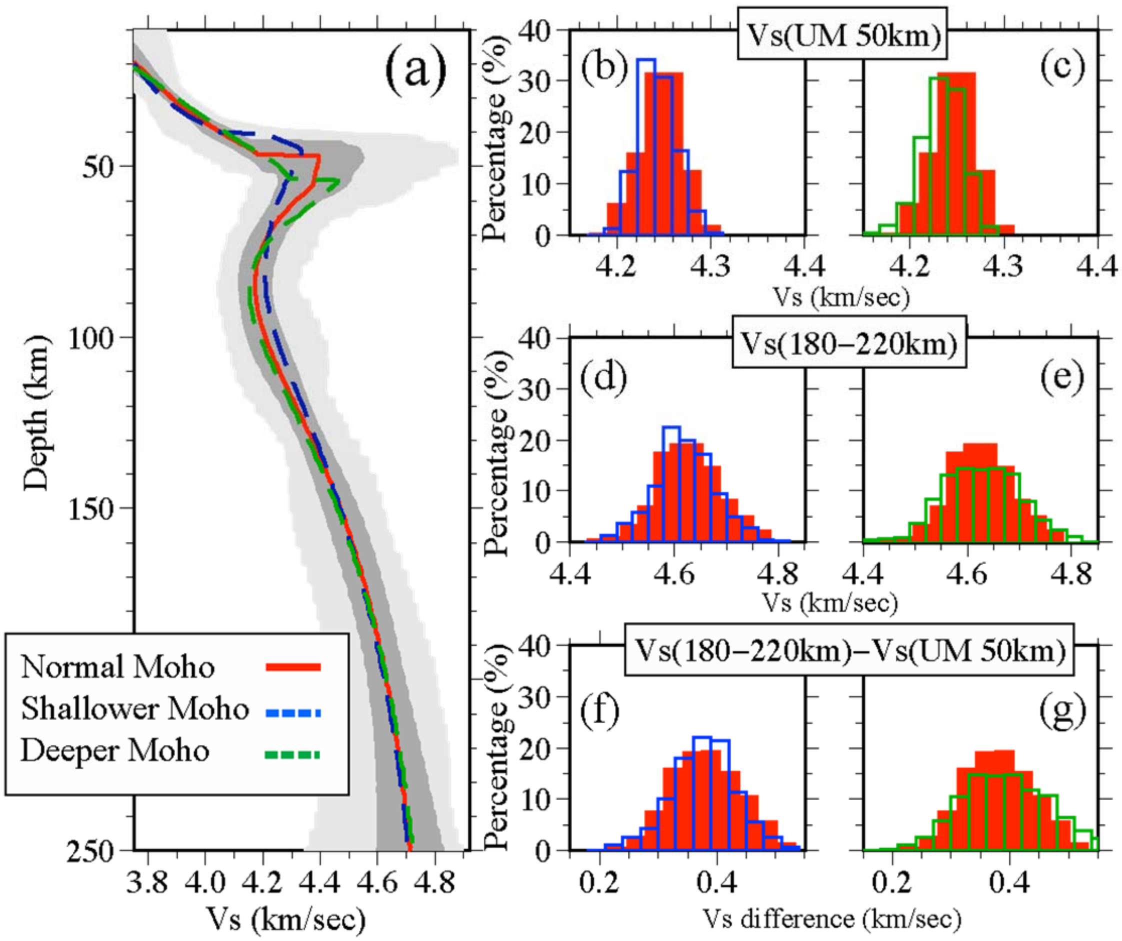


**Supplementary Figure DR8**. Results of the tests from Monte Carlo samplings with different model space. (a) the average model, 1 standard deviation, and full model ensemble for point A whose location is shown in Supp. Fig. DR6a are plotted with red line, dark gray corridor, and light grey corridor, respectively. For comparison, the average models from Monte Carlo sampling performed in a tuned model spaces are shown with dashed lines. Blue dashed line: the model space has a shallower Moho perturbation range (27-47 km). Green dashed line: the model space has a deeper Moho perturbation range (47-67 km). All three average models fit the local surface wave dispersion data at point A. (b-c) Comparison between the three marginal posterior distributions of $V_S$ of the uppermost 50 km of the mantle. Red histogram: for the Monte Carlo sampling with an intermediate Moho depth perturbation range. Blue and green histograms: posterior distribution for Monte Carlo inversions with a shallower and deeper Moho cases, respectively. (f-g). Same as (b-c), but for the difference between $V_S$ (180-220 km) and the $V_S$ of the uppermost 50 km mantle.